ELSEVIER

Volume 215 July 2014 ISSN 0022-4596

JOURNAL OF SOLID STATE CHEMISTRY

IN THIS ISSUE:

Topologically identical, but geometrically isomeric layers in hydrous α-, β-$Rb[UO_2(AsO_3OH)(AsO_2(OH)_2)]\cdot H_2O$ and anhydrous $Rb[UO_2(AsO_3OH)(AsO_2(OH)_2)]$

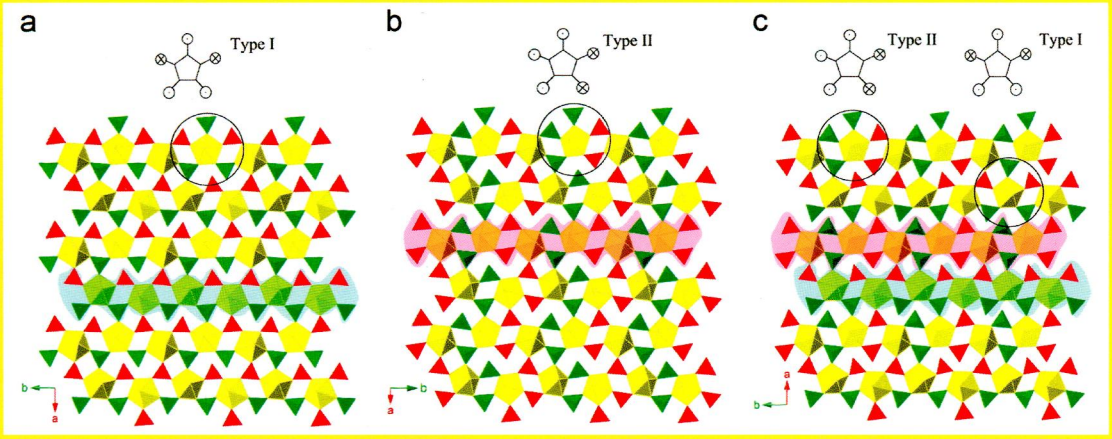

Na Yu, Vladislav V. Klepov, Eric M. Villa, Dirk Bosbach, Evgeny V. Suleimanov, Wulf Depmeier, Thomas E. Albrecht-Schmitt and Evgeny V. Alekseev

Available online at www.sciencedirect.com

ScienceDirect

ELSEVIER

Volume 215, July 2014

CONTENTS

JOURNAL OF SOLID STATE CHEMISTRY

www.elsevier.com/locate/jssc

Abstracted/indexed in BioEngineering Abstracts, Chemical Abstracts, Coal Abstracts, Current Contents/Physics, Chemical, & Earth Sciences, Engineering Index, Research Alert, SCISEARCH, Science Abstracts, and Science Citation Index. Also covered in the abstract and citation database SCOPUS®. Full text available on ScienceDirect®.

Regular Articles

Structural and magnetic characterization of $La_{0.8}Sr_{0.2}MnO_3$ nanoparticles prepared via a facile microwave-assisted method
J. Moradi, M.E. Ghazi, M.H. Ehsani and P. Kameli
page 1

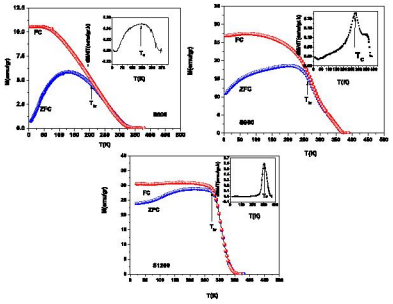

Temperature dependence of the magnetization $M(T)$ was measured in the zero-field-cooling (ZFC) and field-cooling (FC) modes at the applied magnetic field of 100 Oe for the $La_{0.8}Sr_{0.2}MnO_3$ with different size prepared via a facile microwave-assisted method.

Calcination products of gibbsite studied by X-ray diffraction, XPS and solid-state NMR
A. Malki, Z. Mekhalif, S. Detriche, G. Fonder, A. Boumaza and A. Djelloul
page 8

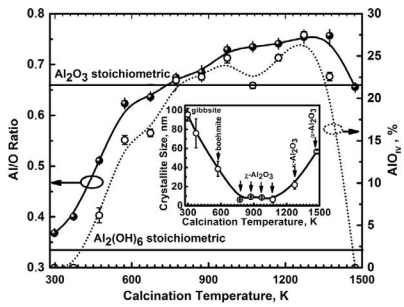

The percentage of AlO_4 units in transition aluminas follows the same behaviour as the ratio of Al/O.

Regular Articles—Continued

Novel high pressure hexagonal OsB_2 by mechanochemistry
Zhilin Xie, Moritz Graule, Nina Orlovskaya, E. Andrew Payzant, David A. Cullen and Richard G. Blair
page 16

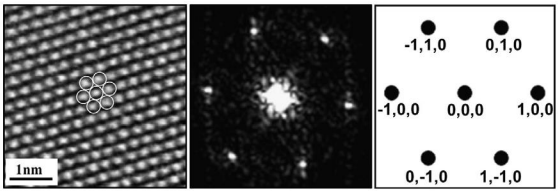

High resolution transmission electron micrograph of hexagonal OsB_2 nanocrystallite with corresponding fast Fourier transform and simulated diffraction pattern.

Visible to near-infrared luminescence properties of Nd^{3+}-doped La_2BaZnO_5 phosphor
Renping Cao, Chunyan Cao, Xiaoguang Yu, Xinyuan Sun, Pengjie Tang and Hui Ao
page 22

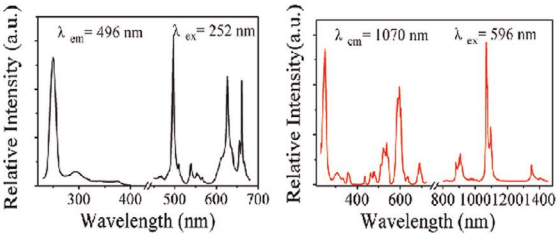

PL spectra of $La_2BaZnO_5:Nd^{3+}$ phosphor in the visible and near-infrared regions and their corresponding to PLE at room temperature.

Continued

Structures and standard molar enthalpies of formation of a series of Ln(III)–Cu(II) heteronuclear compounds with pyrazine-2,3-dicarboxylic acid
Qi Yang, Gang Xie, Qing Wei, Sanping Chen and Shengli Gao
page 26

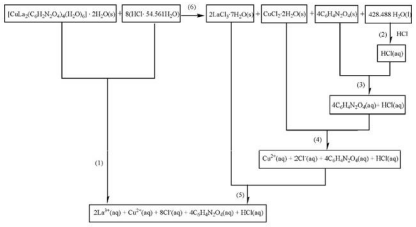

According to Hess' rule, the standard molar enthalpies of formation of Ln–Cu heterometallic coordination compounds were determined by a designed thermochemical cycle.

Secondary ligand-directed assembly of Co(II) coordination polymers based on a pyridine carboxylate ligand
Ke-Li Cao, Yi-Ping Zhang, Yi-Ni Cai, Xiao-Wei Xu and Yun-Long Feng
page 34

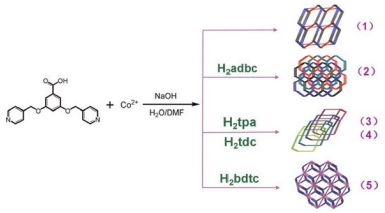

The structural differences show that the ancillary ligands have great effects on the spatial connective fashions, resulting in the formation of various dimensional compounds.

Effects of Pd substitution on the thermoelectric and electronic properties of delafossite $Cu_{1-x}Pd_xFeO_2$ (x=0.01, 0.03 and 0.05)
Chesta Ruttanapun
page 43

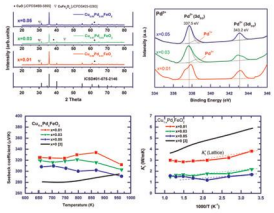

$Cu_{(1-x)}Pd_{(x)}FeO_2$ (x=0.01, 0.03 and 005) delafossite was prepared by solid state reactions. The characterization showed that $Cu_{(1-x)}Pd_{(x)}FeO_2$ formed a hexagonal delafossite structure with $R3{-}m$ symmetry. The existence of Pd^{2+}, Cu^{1+}, Cu^{2+}, Fe^{3+}, Fe^{4+} and O was revealed from the XPS results. The O content intercalated at the center of the triangular Cu acted as a support to produce Cu^{2+} ions and was reduced with an increasing Pd content. The mixed valencies of Cu^{1+}/Cu^{2+} and Cu^{1+}/Pd^{2+} in the Cu layer changed the electrical conductivity and the Fe^{3+}/Fe^{4+} mixed valencies in the FeO_6 layer caused the Seebeck coefficient to increase. Both the electrical conductivity and Seebeck coefficient for Pd contents of x=0.01 and 0.03 were higher than that of non-doped $CuFeO_2$. The low thermal conductivity of $Cu_{(1-x)}Pd_{(x)}FeO_2$ resulted from the substitution of Pd, which has a large atomic mass, into structure. A high ZT value of 0.055 was obtained for a Pd content of 0.03 at 950 K. The Pd^{2+} substitution for the Cu^{1+} sites influenced the thermoelectric and electronic properties of the delafossite $Cu_{(1-x)}Pd_{(x)}FeO_2$ samples.

Solid-state actinide acid phosphites from phosphorous acid melts
George N. Oh and Peter C. Burns
page 50

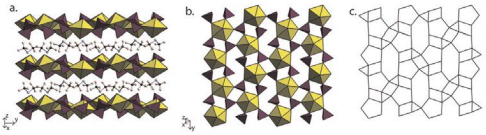

Reaction of UO_3 and H_3PO_3 at 100 °C and subsequent reaction with DMF produces crystals of $(NH_2(CH_3)_2)[UO_2(HPO_2OH)(HPO_3)]$ with a layered structure. Reaction of phosphorous acid and actinide oxides at 210 °C produces a viscous syrup and further solution-state reactions result in the crystallization of the actinide acid phosphites $An(HPO_2OH)_4$ (An=U, Th), with a three-dimensional network structure, and the mixed acid phosphite–phosphite $U(HPO_3)(HPO_2OH)_2(H_2O)_2{\cdot}(H_2O)$ with a layered structure.

New organic–inorganic hybrid assemblies based on copper (I) ion, bichelate-bridging ligand and Lindqvist-type polyoxometalate
Mao-Mao Zhang, Xiu-Li Hao, Li-Jie Xu, Yong-Hui Wang, Xin Wang and Yang-Guang Li
page 57

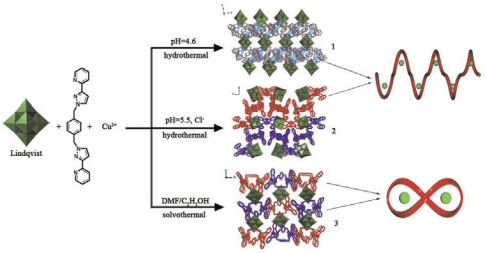

Three new hybrid compounds based on same Cu(I) ion, bichelate-bridging ligand and $[W_6O_{19}]^{2-}$ building blocks were synthesized. Various structural features of three compounds were tuned by different synthetic conditions.

Controllable synthesis of hollow mesoporous silica spheres and application as support of nano-gold
Tao Wang, Weihua Ma, Junnan Shangguan, Wei Jiang and Qin Zhong
page 67

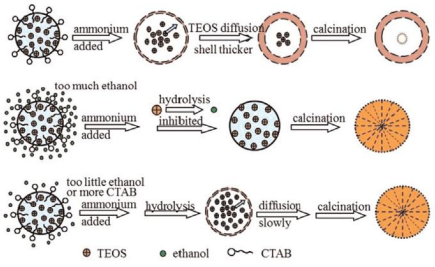

It is the schematic mechanism for the formation of hollow mesoporous silica spheres.

Layered zirconium phosphonate with inorganic–organic hybrid structure: Preparation and its assembly with DNA
Li-Min Liu, Guo-Yuan Lu, Li-Ping Jiang and Jun-Jie Zhu
page 74

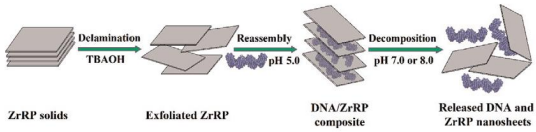

The intercalation of DNA into zirconium phosphonate and the release of DNA from the interlayer of zirconium phosphonate.

Structural and property studies on metal–organic compounds with 3-D supramolecular network
Qi-Ying Zhang, Ke-Fang Ma, Hong-Ping Xiao, Xin-Hua Li and Qian Shi
page 80

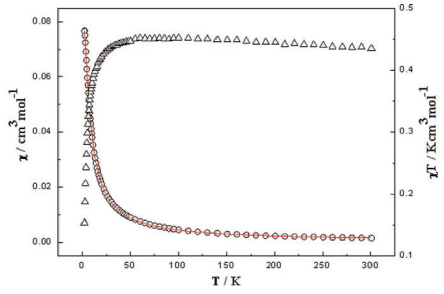

Variable-temperature magnetic property studies of two 3-D supramolecular compounds reveal the existence of antiferromagnetic interactions between the metal ions, through the effective super-exchange media.

New insights into the enigma of boron carbide inverse molecular behavior
Przemyslaw Dera, Murli H. Manghnani, Anwar Hushur, Yi Hu and Sergey Tkachev
page 85

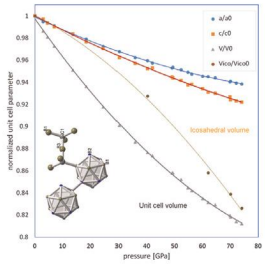

Single crystal measurements of equation of state and compression mechanism of B_4C show that the icosahedral units are less compressibe than the unit cell volume, despite the threei-ceneterd nature of some icosahedral bonds.

A novel nano-sized BiOBr decorated $K_2La_2Ti_3O_{10}$ with enhanced photocatalytic properties under visible light
Wenquan Cui, Weijia An, Li Liu, Jinshan Hu and Yinghua Liang
page 94

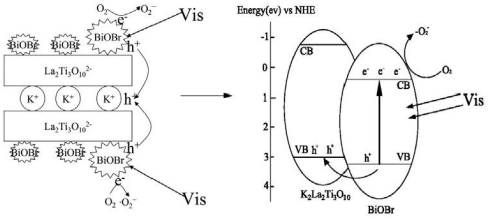

Photocatalytic reaction mechanisms of the as-prepared BiOBr/$K_2La_2Ti_3O_{10}$.

Variations of structures and solid-state conductivity of isomeric silver(I) coordination polymers having linear and *V*-shaped thiophene-centered ditriazole ligands
Bin Hu, Jiao Geng, Lie Zhang and Wei Huang
page 102

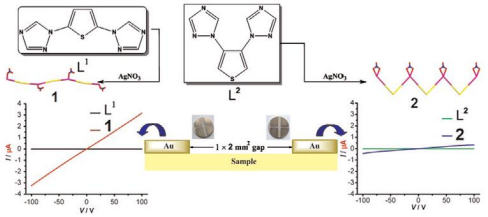

A pair of linear and *V*-shaped isomeric thiophene-centered ditriazole ligands (L^1) and L^2 are used to prepare a pair of silver(I) polymeric isomers (**1** and **2**), where significant enhancement of solid-state conductivity to different extents are observed originating from the distinguishable shape and configuration of isomeric ligands.

Effects of isomorphous substitution of a coordination polymer on the properties and its application in electrochemical sensing
Bo Zhou, Li-Mei Liang and Jie Yao
page 109

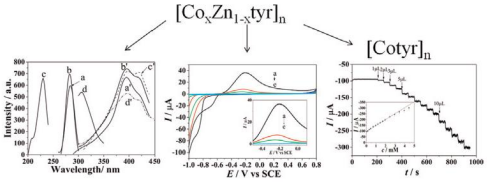

Evolution of the optical and electrochemical properties of isomorphic coordination polymers $[Co_xZn_{1-x}tyr]_n$ along with the changing of x was studied. The CP also showed perfect performance in the electrochemical determination of nitrite.

Continued

Structure and physical properties of RT_2Cd_{20} (R=rare earth, T=Ni, Pd) compounds with the $CeCr_2Al_{20}$-type structure

V.W. Burnett, D. Yazici, B.D. White, N.R. Dilley, A.J. Friedman, B. Brandom and M.B. Maple

page 114

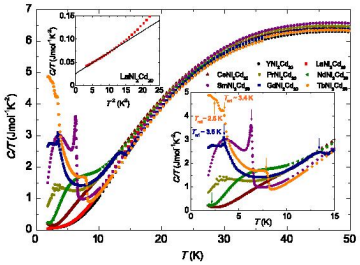

Specific heat divided by temperature C/T vs. T for single crystals of R Ni_2Cd_{20} (R=Y, La–Nd, Gd, and Tb). Left inset: Low temperature C/T vs. T^2 for $LaNi_2Cd_{20}$. The solid line represents a linear fit of the data. Right inset: Low-temperature C/T data vs. T for R=Ce–Nd, Gd, and Tb; magnetic ordering temperatures are indicated by arrows.

Mg dopant in $Cu_2ZnSnSe_4$: An n-type former and a promoter of electrical mobility up to 120 cm^2 V^{-1} s^{-1}

Dong-Hau Kuo and Walelign Wubet

page 122

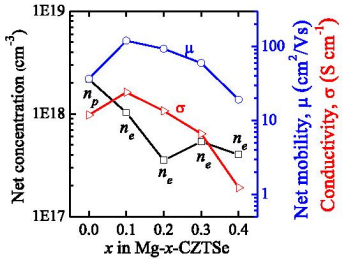

The effects of extrinsic doping of Mg^{2+} on the electrical properties of $Cu_2ZnSnSe_4$ bulks.

Phase equilibria and crystal chemistry of the CaO–$\frac{1}{2}Nd_2O_3$–CoO_z system at 885 °C in air

W. Wong-Ng, W. Laws, K.R. Talley, Q. Huang, Y. Yan, J. Martin and J.A. Kaduk

page 128

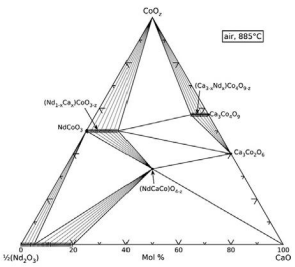

Phase diagram of the $\frac{1}{2}Nd_2O_3$–CaO–CoO_x system at 885 °C, showing the limits of various solid solutions, and the tie-line relationships of various phases.

Self-assembled ultra small ZnO nanocrystals for dye-sensitized solar cell application

Astam K. Patra, Arghya Dutta and Asim Bhaumik

page 135

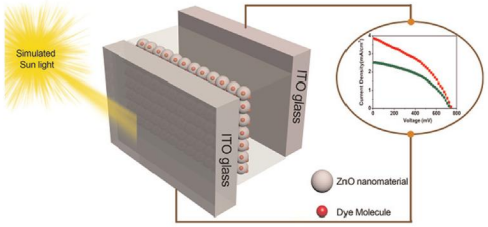

Ultra-small ZnO nanocrystals have been synthesized with sodium salicylate as a template and using it as a photoanode in a dye-sensitized solar cell 1.12% power conversion efficiency has been observed.

Novel ethylenediamine-gallium phosphate containing 6-fold coordinated gallium atoms with unusual four equatorial Ga–N bonds

Laura Torre-Fernández, Aránzazu Espina, Sergei A. Khainakov, Zakariae Amghouz, José R. García and Santiago García-Granda

page 143

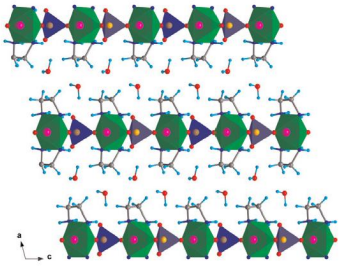

Single crystals of a new ethylenediamine-gallium phosphate, $Ga(H_2NCH_2CH_2NH_2)_2PO_4{\cdot}2H_2O$, were obtained and the structural features presented. This structure is one of the scarce examples of GaPO with Ga–N bonds reported.

Topologically identical, but geometrically isomeric layers in hydrous α-, β-$Rb[UO_2(AsO_3OH)(AsO_2(OH)_2)]{\cdot}H_2O$ and anhydrous $Rb[UO_2(AsO_3OH)(AsO_2(OH)_2)]$

Na Yu, Vladislav V. Klepov, Eric M. Villa, Dirk Bosbach, Evgeny V. Suleimanov, Wulf Depmeier, Thomas E. Albrecht-Schmitt and Evgeny V. Alekseev

page 152

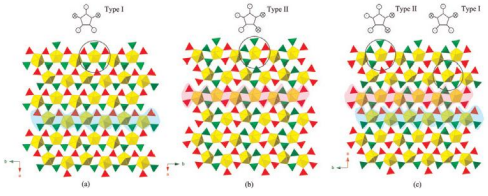

Three different layer geometries observed in the structures of $Rb[UO_2(AsO_3OH)(AsO_2(OH)_2)]$ and α- and β- $Rb[UO_2(AsO_3OH)(AsO_2(OH)_2)]{\cdot}H_2O$. Two different coordination environments of uranium polyhedra (types I and II) are shown schematically on the top of the figure.

Synthesis of MnO_2-graphene composites with enhanced supercapacitive performance via pulse electrodeposition under supergravity field

Tingting Liu, Guangjie Shao, Mingtong Ji and Guiling Wang

page 160

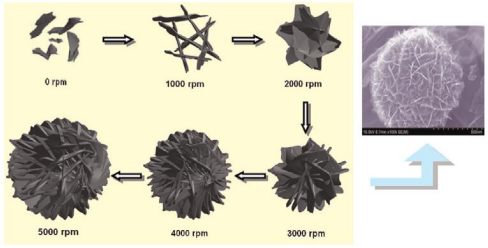

3D flower like MnO_2 spheres composed of nanoflakes were acquired at 3000 rpm.

Effects of Au content on the structure and magnetic properties of $L1_0$-FePt nanoparticles synthesized by the sol–gel method

Yang Liu, Yuhong Jiang, Naveen Kadasala, Xiaolong Zhang, Chenyi Mao, Yaxin Wang, Huilian Liu, Yanqing Liu, Jinghai Yang and Yongsheng Yan

page 167

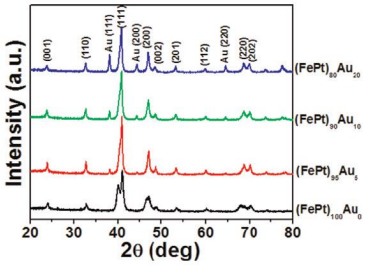

$(FePt)_{100}Au_0$ NPs are the coexistence of FCT and FCC phases. However, no hints of FCC phase were found for the $(FePt)_{100-x}Au_x$ NPs (x=5, 10 and 20), which indicates that addition of gold greatly promotes the FCC to FCT phase transition.

Magnetic ordering in the pyrochlore Ho_2CrSbO_7 determined from neutron diffraction, and the magnetic properties of other RE_2CrSbO_7 phases (RE=Y, Tb, Dy, Er)

Mariana J. Whitaker and Colin Greaves

page 171

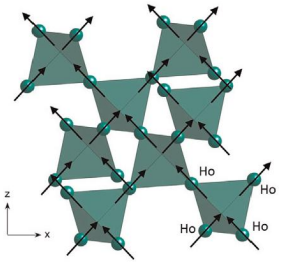

The Ho magnetic moments align to provide an overall ferromagnetic moment along [001].

Synthesis and crystal structure characterization of $InGaZnO_4$ with a new defect structure

W. Assenmacher, G. Schnakenburg, Y. Michiue, Y. Kanke, N. Kimizuka and W. Mader

page 176

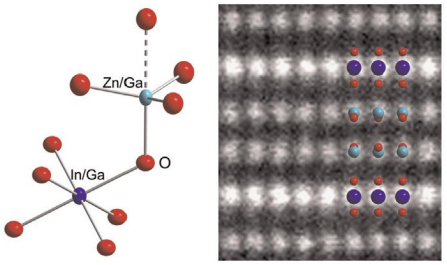

Single crystals of $InGaZnO_4$ have been synthesized at ambient pressure and analyzed with X-ray diffraction, electron microscopy, and optical absorption. Optical band gap and optical transmission have been determined.

Synchrotron X-ray powder diffraction and convergent beam electron diffraction studies on the cubic phase of MgV_2O_4 spinel

Seiji Niitaka, Soyeon Lee, Yoshifumi Oshima, Kenichi Kato, Daisuke Hashizume, Masaki Takata and Hidenori Takagi

page 184

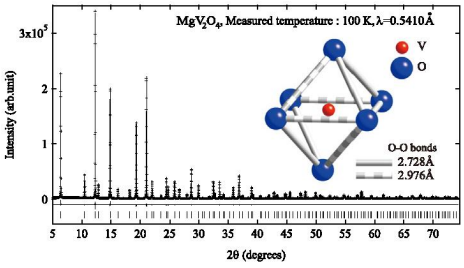

Precise geometry of the VO_6 octahedra in the cubic phase of MgV_2O_4 spinel determined with the synchrotron powder XRD data

---

Anisotropic magnetic behaviors of monoclinic $Li_3Fe_2(PO_4)_3$

Zhangzhen He, Wenbin Guo, Wendan Cheng and Mitsuru Itoh

page 189

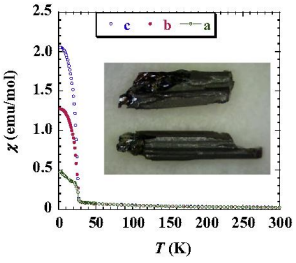

Magnetic anisotropy is confirmed for the first time using a single crystal sample of α-$Li_3Fe_2(PO_4)_3$ obtained by the flux method.

Continued

Behavior of the magnetocaloric effect and critical exponents in $La_{0.67}Sr_{0.33}Mn_{1-x}V_xO_3$ manganite oxide
S. Mnefgui, N. Zaidi, A. Dhahri, E.K. Hlil and J. Dhahri
page 193

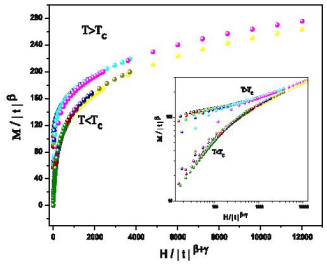

Scaling plot below and above T_C using the β and γ exponents determined from the Arrot plot method of $La_{0.67}Sr_{0.33}Mn_{1-x}V_xO_3$ for x=0.15.

Preparation and characterization of pitch-based nanoporous carbons for improving CO_2 capture
Seul-Yi Lee, Hye-Min Yoo, Sang Wook Park, Sang Hee Park, Young Se Oh, Kyong Yop Rhee and Soo-Jin Park
page 201

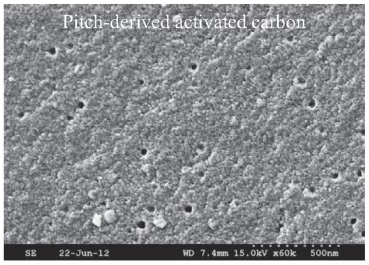

This is the surface morphologies of pitch precursor and pitch-derived activated carbon (AC-2).

Synthesis, structure refinement and chromate sorption characteristics of an Al-rich bayerite-based layered double hydroxide
Sylvia Britto and P. Vishnu Kamath
page 206

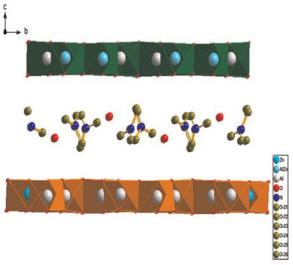

The structure of the [Zn–Al4-nitrate] LDH viewed along the a-axis.

Influence of calcination parameters on the synthesis of N-doped TiO_2 by the polymeric precursors method
Margaret Dawson, Gabriela Byzynski Soares and Caue Ribeiro
page 211

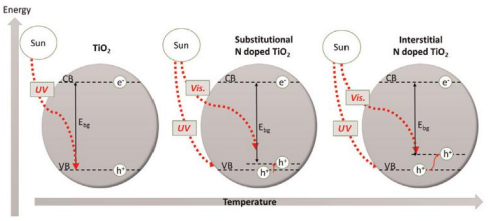

The temperature influences to promote higher quantities of Interstitial N doped TiO_2 than Substitutional and due to difference between energies levels for substitutional N doped TiO_2 and Interstitial N doped TiO_2, it is presented difference on photocatalytic activity.

Improvement of thermoelectric properties induced by uniquely ordered lattice field in $Bi_2Se_{0.5}Te_{2.5}$ pillar array
Ming Tan, Yanming Hao and Gangzhi Wang
page 219

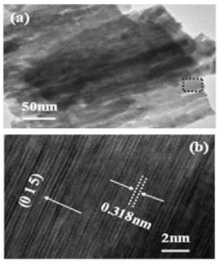

In this study, it was found that uniquely ordered lattice field favors transport of carriers but hinder that of phonons. The $Bi_2Se_{0.5}Te_{2.5}$ pillar array film with a thermoelectric dimensionless figure-of-merit ZT=1.28 was obtained at room temperature. The in-plane transport mechanisms of the ordered pillar array and the ordinary structures, the lattice field model, are proposed and investigated. The specially ordered lattice field is the main reason for the properties enhancement observed in the $Bi_2Se_{0.5}Te_{2.5}$ pillar array. Introduction of such uniquely ordered lattice field into TE films is therefore a very promising approach. In (a) TEM and (b) HRTEM images of the ordered $Bi_2Se_{0.5}Te_{2.5}$ column array.

High-temperature behavior of dicesium molybdate Cs_2MoO_4: Implications for fast neutron reactors
Gilles Wallez, Philippe E. Raison, Anna L. Smith, Nicolas Clavier and Nicolas Dacheux
page 225

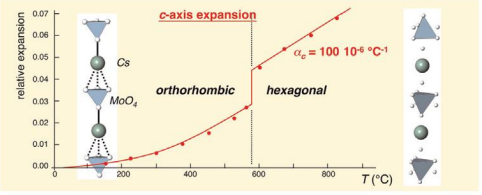

The weakness of the Cs–O bonds and the disordering of the MoO_4 tetrahedra array in the high-temperature form are responsible for the huge thermal expansion of Cs_2MoO_4 along the c-axis.

Nanostructured rocksalt-type solid solution series $(Ge_{1-x}Sn_xTe)_nSb_2Te_3$ (n=4, 7, 12; $0 \le x \le 1$): Thermal behavior and thermoelectric properties
Tobias Rosenthal, Lukas Neudert, Pirmin Ganter, Johannes de Boor, Christian Stiewe and Oliver Oeckler
page 231

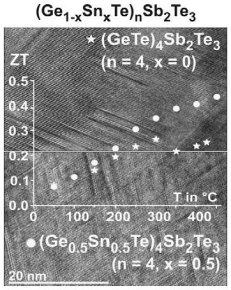

High-resolution transmission electron micrographs of $(GeTe)_4Sb_2Te_3$ (top) and $(Ge_{0.5}Sn_{0.5}Te)_4Sb_2Te_3$ (bottom) with different nanostructures and thermoelectric figures of merit (ZT) of these samples.

Magnetic properties of pseudo-ideal cubic $La_{0.6-x}Ca_xBa_{0.4}CoO_3$ with hole doping
Hong Chang, Qiang Wu and Pengwei Ge
page 241

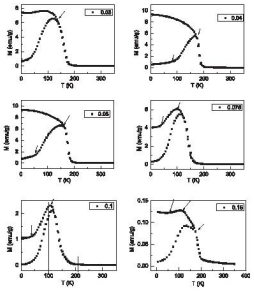

The thermal magnetization at 200 Oe at the ZFC and the FC states.

$Pb_5Fe_3TiO_{11}Cl$: A rare example of Ti(IV) in a square pyramidal oxygen coordination
Maria Batuk, Dmitry Batuk, Artem M. Abakumov and Joke Hadermann
page 245

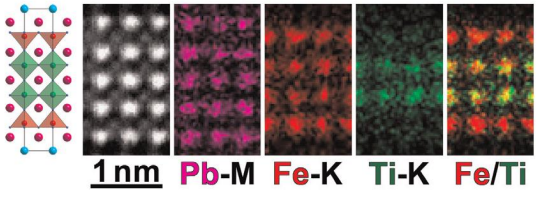

The beneficial influence of tellurium on the thermoelectric properties of $Mo_{3-x}Fe_xSb_7$
Quansheng Guo and Holger Kleinke
page 253

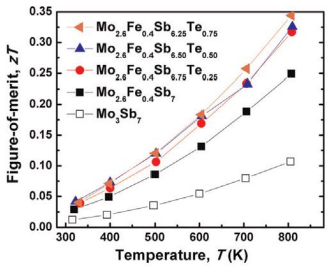

Figure-of-merit of $Mo_{3-x}Fe_xSb_{7-y}Te_y$.

Influence of oxide impurities on the chemical tuning of the thermoelectric properties of substitution derivatives of $RuIn_3$
Maik Wagner-Reetz, Raul Cardoso-Gil, Marcus Schmidt and Yuri Grin
page 260

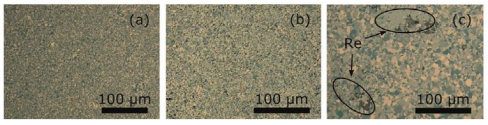

Microstructure (perpendicular to the pressure axis; polarized light) of polycrystalline $Ru_{0.95}Rh_{0.05}In_3$ (a), $Ru_{0.95}Ir_{0.05}In_3$ (b) and $Ru_{0.95}Re_{0.05}In_3$ (c) samples after SPS treatment.

Phase transformation of $Ca_4[Al_6O_{12}]SO_4$ and its disordered crystal structure at 1073 K
Daisuke Kurokawa, Seiya Takeda, Maggy Colas, Toru Asaka, Philippe Thomas and Koichiro Fukuda
page 265

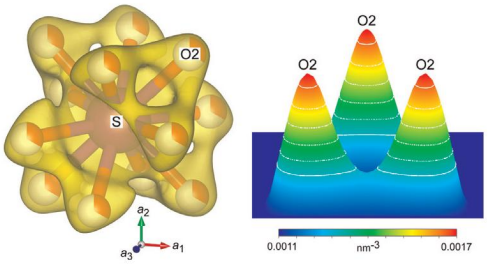

(Left) Three-dimensional electron-density distributions of the SO_4 tetrahedron with the split-atom model, and (right) a bird's eye view of electron densities on the plane parallel to (111).

Continued

Magnetic and magnetocaloric properties of $La_{0.6}Pr_{0.1}Sr_{0.3}Mn_{1-x}Fe_xO_3$ ($0 \le x \le 0.3$) manganites
R. Cherif, E.K. Hlil, M. Ellouze, F. Elhalouani and S. Obbade
page 271

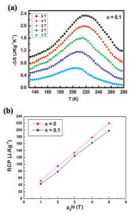

Magnetic entropy change versus temperature and applied magnetic field for x=0.1 (a) and RCP versus applied magnetic field for x=0, 0.1 (b).

Different dimensional coordination polymers with 4,4'-oxybis(benzoate): Syntheses, structures and properties
Huijie Lun, Yamin Li, Xudong Zhang, Jing-He Yang, Changyu Xiao, Yanqing Xu and Junrui Li
page 277

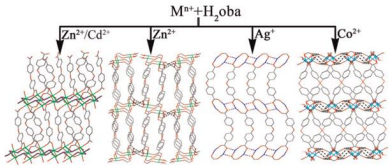

Five new transition-metal coordination complexes **1**–**5** have been synthesized and characterized by single-crystal X-ray diffractions, IR spectra, elemental analyses, thermogravimetric analyses (TGA), photoluminescent spectra and magnetic measurement.

Chemical design of pH-sensitive nanovalves on the outer surface of mesoporous silicas for controlled storage and release of aromatic amino acid
N.V. Roik and L.A. Belyakova
page 284

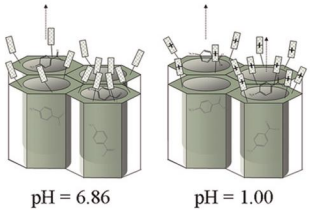

Blocking of pores with N-[N′-(N′-phenyl)-2-aminophenyl]-3-aminopropyl groups at pH=6.86 for storage of ABA and opening of pore entrances at pH=1.00 for unhindered ABA liberation.

Copper(II) complexes with 4-(1*H*-1, 2, 4-trizol-1-ylmethyl) benzoic acid: Syntheses, crystal structures and antifungal activities
Pingping Xiong, Jie Li, Huaiyu Bu, Qing Wei, Ruolin Zhang and Sanping Chen
page 292

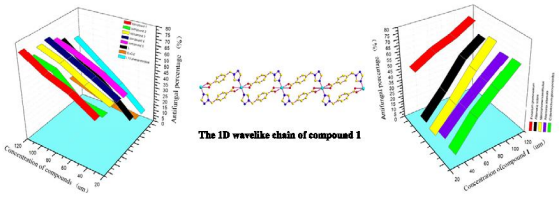

Copper(II) compounds with 4-(1*H*-1, 2, 4-trizol-1-ylmethyl) benzoic acid, were prepared, structurally characterized and investigated for antifungal activity.

Synthesis of murdochite-type Ni_6MnO_8 with variable specific surface areas and the application in methane oxidation
Hideki Taguchi, Shohei Tahara, Mikoto Okumura and Ken Hirota
page 300

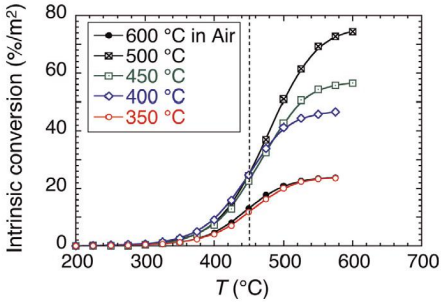

The conversion of CH_4 into CO_2 and H_2O on Ni_6MnO_8, which was heated at 600 °C in air after the calcination of the precursor at 350 °C, 400 °C, 450 °C, or 500 °C in flowing argon, was measured. Since the specific surface area was strongly affected by the calcination temperature of the precursor, intrinsic conversion (*IC*) was defined as conversion per the specific surface area. For comparison, the *IC* value on Ni_6MnO_8 synthesized by the direct calcination of the precursor at 600 °C in air is plotted.